

Origin and Quantitative Description of the NESSIAS Effect at Si Nanostructures

Dirk König,¹ Michael Frentzen,² Daniel Hiller,³ Noël Wilck,² Giovanni Di Santo,⁴ Luca Petaccia,⁴ Igor Píš,⁵ Federica Bondino,⁵ Elena Magnano,⁵ Joachim Mayer,⁶ Joachim Knoch,² and Sean C. Smith⁷

¹*Integrated Materials Design Lab (IMDL), The Australian National University, ACT 2601 Canberra, Australia**

²*Institute of Semiconductor Electronics (IHT), RWTH Aachen University, 52074 Aachen, Germany*

³*Institute of Applied Physics (IAP), Technische Universität Bergakademie Freiberg, 09599 Freiberg, Germany*

⁴*Elettra Sincrotrone Trieste, Strada Statale 14 km 163.5, 34149 Trieste, Italy*

⁵*IOM-CNR, Istituto Officina dei Materiali, Area Science Park S.S. 14 km 163.5, 34149 Trieste, Italy[†]*

⁶*Ernst-Ruska Centre for Microscopy and Spectroscopy with Electrons, RWTH Aachen University, 52074, Germany*

⁷*Department of Applied Mathematics, Research School of Physics and Engineering, The Australian National University, ACT 2601 Canberra, Australia[‡]*

The electronic structure of low nanoscale (LNS) intrinsic silicon (i-Si) embedded in SiO₂ *vs.* Si₃N₄ shifts away from *vs.* towards the vacuum level E_{vac} , as described by the Nanoscale Electronic Structure Shift Induced by Anions at Surfaces (NESSIAS). Here, we fully explain the NESSIAS based on the quantum chemical properties of the elements involved. Deriving an analytic parameter Λ to predict the highest occupied molecular orbital energy of Si nanocrystals (NCs), we use various hybrid-DFT methods and NC sizes to verify the accuracy of Λ . We report on first experimental data of Si nanowells (NWells) embedded in SiO₂ *vs.* Si₃N₄ by X-ray absorption spectroscopy in total fluorescence yield mode (XAS-TFY) which are complemented by ultraviolet photoelectron spectroscopy (UPS), characterizing their conduction band and valence band edge energies E_C and E_V , respectively. Scanning the valence band sub-structure by UPS over NWell thickness, we derive an accurate estimate of E_V shifted purely by spatial confinement, and thus the actual E_V shift due to NESSIAS. For 1.9 nm thick NWells in SiO₂ *vs.* Si₃N₄, we get offsets of $\Delta E_C = 0.56$ eV and $\Delta E_V = 0.89$ eV, demonstrating a type II homojunction in LNS i-Si. This p/n junction generated by the NESSIAS eliminates any deteriorating impact of impurity dopants, offering undoped ultrasmall Si electronic devices with much reduced physical gate lengths and CMOS-compatible materials.

I. INTRODUCTION

Silicon (Si) nanowells (NWells) with a thickness of $d_{\text{Well}} \leq \text{ca. } 3.3$ nm embedded in silicon dioxide (SiO₂) *vs.* silicon nitride (Si₃N₄) show an electronic structure shift with respect to the vacuum energy level E_{vac} as measured by ultraviolet photoelectron spectroscopy (UPS) and X-ray absorption spectroscopy in total fluorescence yield mode (XAS-TFY) [1–3]. NWells embedded in SiO₂ (Si₃N₄) get shifted to higher (lower) binding energies, that is, away from (towards to) E_{vac} . This Nanoscopic Electronic Structure Shift Induced by Anions at Surfaces (NESSIAS) effect is caused by quantum chemical properties of the anions forming the dielectric which surrounds the low nanoscale (LNS) Si. While the NESSIAS effect has been established in theory and experiment, its exact origin and quantitative description are still elusive. Here, we deliver a detailed quantum chemical explanation of the NESSIAS effect, complemented with its semi-quantitative description which serves to predict NESSIAS in LNS intrinsic Si (i-Si) for a variety of anions in embedding/coating dielectrics. To this end, we pro-

vide experimental evidence and details of the quantum-chemical concept which leads to the NESSIAS effect.

The NESSIAS effect induces a p/n junction on semiconductor nanostructures such as fins, nanowires (NWires), or nanocrystals (NCs) by enabling an electron flooding of the nanostructure when coated with SiO₂ [3], or a virtually complete electron drainage from the nanostructure when coated with Si₃N₄ [1, 2], introducing a high density of holes into the nanovolume by the latter process. This re-arrangement of charge carrier densities has far-reaching consequences for semiconductor devices in very large scale integration (VLSI), ultra-low power and cryo-electronics. Spatial fluctuations of dopant densities, out-diffusion and self-purification impose a size limit onto VLSI devices as evident from *physical* gate lengths hovering around 20 nm since ca. 2014 [4]. With thermal dopant ionization not required, junctions induced by the NESSIAS effect should remain fully functional down to extremely low temperatures as useful for peripheral electronics in qbit manipulation [5].

The detection of the NESSIAS in LNS i-Si requires an absolute assignment of energies to E_{vac} , combined with elaborate UPS and XAS-TFY measurements and refined data processing for improved signal-to-noise ratios [1–3]. To this end, the structures under investigation have to be in the range of the NESSIAS impact length. Many published DFT calculations [6–9] lack an energy assignment on an absolute scale. Possibly identical LNS i-Si NWell systems near the low end of the one-digit nm range embedded in different dielectrics pose a challenge in exper-

* Smart Materials and Surface Group, University of New South Wales, NSW 2052 Sydney, Australia; solidstatedirk@gmail.com

[†] E. Magnano: Department of Physics, University of Johannesburg, PO Box 524, Auckland Park 2006, South Africa

[‡] Integrated Materials Design Lab (IMDL), The Australian National University, ACT 2601 Canberra, Australia

iment. The common perception of Si_3N_4 as an inferior dielectric on grounds of interface defect density [10] and its more complex technology as opposed to SiO_2 [11] are likely reasons for the literature on LNS Si embedded in or coated with Si_3N_4 being rather scarce. Indeed, standard Si_3N_4 has an interface defect density to LNS Si which exceeds values of SiO_2/Si interfaces *ca.* 13-fold [10, 12, 13], though refined preparation techniques for high-quality H-passivated Si_3N_4 -coatings rival trap densities on SiO_2/Si interfaces [14]. This complex situation may explain why the NESSIAS might have been overlooked in the past.

After introducing the methods used in Section II, we deliver a phenomenological and qualitative explanation of the NESSIAS effect in Section III A, resorting to quantum chemical properties of involved chemical elements. In Section III B, we derive a semi-quantitative analytic parameter Λ of the NESSIAS effect to describe the energy of the highest occupied molecular orbital (HOMO) E_{HOMO} as a function of anion-specific quantum chemical properties combined with the charge of these main anions q_{main} of the ligand groups attached to Si NCs. In Section III C, we test Λ with a variety of density functionals (DFs) and most anionic elements of the first and second row of the periodic table with respect to Si, subject to the availability of experimental quantum chemical data. Our discussion is complemented with synchrotron data in Section III D. Since the electronic structure of NWells shifts as a function of quantum confinement (QC), it is essential to separate this phenomenon induced by a *spatial* limit from the NESSIAS brought about by the quantum-chemical nature of embedding dielectric *vs.* Si. To this end, we evaluate our results from synchrotron UPS measurements in Section III D 1, revealing sub-structures of the valence band which serve to estimate the actual QC. This true QC is revealed by the shift of the valence band (VB) edge to higher binding energies as a sole function of NWell thickness, occurring in all samples irrespective of the embedding dielectric. We use this VB edge as a reference level to estimate the *actual* NESSIAS as per embedding dielectric in the QC regime. Next, we evaluate our experimental data of the VB and conduction band (CB) edges as measured by synchrotron XAS-TFY in Section III D 2, establishing the link between bulk Si and SiO_2 *vs.* Si_3N_4 as given by ultrathin Si NWells coated with the respective dielectric. Section IV delivers a conclusion.

II. METHODS

A. Sample Preparation

After determining the Deal-Grove parameters [15] for the furnace oxidation of silicon-on-insulator (SOI) samples, the SOI crystalline Si (c-Si) layers (p-type, $1 \Omega\text{cm}$) on Si wafers with 145 nm buried SiO_2 (BOx) were oxidized down to a thickness of 2.1 to 6.0 nm. The SiO_2 was removed by etching in a buffered oxide etch (BOE; 1 wt-% HF buffered with NH_4F), followed by a self-limiting

oxidation in 68 wt-% HNO_3 at 120 °C, yielding a 1.1 to 5.0 nm Si-NWell with 1.4 nm SiO_2 capping. A lateral metal contact frame was processed on the front surface by photolithographical structuring, wet-chemical etching in BOE for opening the top SiO_2 layer and thermal evaporation of 300 nm Al, followed by a lift-off in acetone. The Si reference samples were contacted directly on their front surface. NWell samples were coated with photo resist immediately after NWell thickness measurements using Mueller matrix ellipsometry straight after processing to prevent oxidation in air. Resist was removed just prior to sample mounting at the beamline. Si reference samples consisted of (001)-Si wafer (Sb-doped *n*-type, $0.01 \Omega\text{cm}$) which were treated with a BOE immediately before sample mounting under a N_2 gas flow with swift loading into the ultra-high vacuum (UHV) annealing chamber.

Si-NWells in Si_3N_4 were processed in analogy to the ones in SiO_2 , using the same SOI wafers as starting point. The SOI was thinned down to a remanent Si device layer which was 1 nm thicker than the final NWell thickness, accommodating for Si consumption during the growth of Si_3N_4 . Next, the SiO_2 capping is removed with BOE immediately before growing 3 nm of Si_3N_4 in an ammonia atmosphere by rapid thermal nitridation (RTN). Afterwards, 20 nm of Si_3N_4 and 80 nm of SiO_2 were deposited by plasma enhanced chemical vapor deposition, followed by chemical mechanical polishing of the SiO_2 layer. After an RCA clean [16], the samples were bonded to a Si sample [17] covered by SiO_2 of *ca.* 1.5 nm thickness which was grown during RCA-SC2 step. The original Si substrate of the SOI samples was etched back using a cyclic deep reactive ion etching process based on passivation with C_4F_8 and etching with SF_6 . The BOx served as a stopping layer and was subsequently removed by a BOE immediately before growing 1 nm of Si_3N_4 by RTN in ammonia atmosphere. Contacts to the NWells were fabricated by photolithography, etching the Si_3N_4 with 1 wt-% hydrofluoric acid and deposition of 300 nm Al.

The layout of the samples and a high resolution TEM image of a NWell sample is shown Fig. 1.

B. Characterization

For synchrotron-based characterization techniques such as X-ray absorption spectroscopy measurements in total fluorescence yield (XAS-TFY) and UV photoelectron spectroscopy (UPS), all samples were subject to a UHV anneal for 60 min at 500 K to desorb water and air-related species from the sample surface prior to measurements. Synchrotron XAS-TFY measurements were carried out at the BACH CNR beamline [18, 19] at the Elettra synchrotron radiation facility in Trieste, Italy, in top-up mode at an electron energy of 2.4 GeV (140 mA electron ring current). The photon energy scale has been calibrated using the energy position of the Si L3-edge (99.6 eV) measured on a reference (001)-Si wafer. A multitude of spectra was recorded per sample to obtain

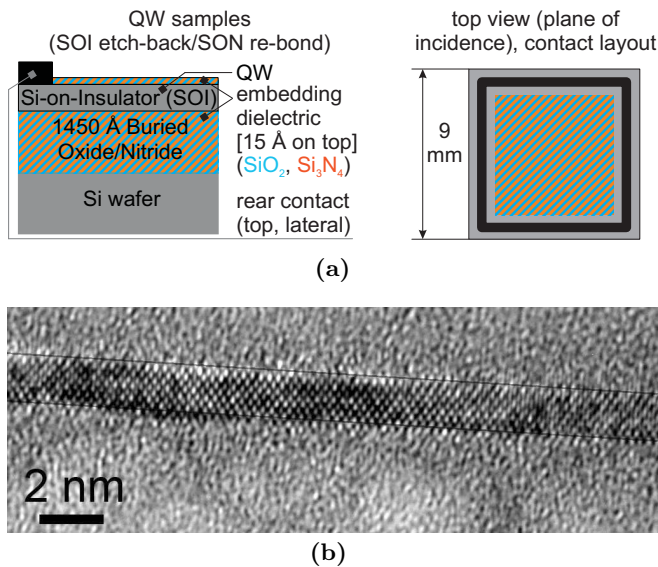


FIG. 1. Layout of Si_3N_4 - and SiO_2 -embedded Si NWell samples for synchrotron UPS and XAS-TFY, shown in X-section and top view (a). X-section view of 1.5 nm (001)-Si NWell in Si_3N_4 as obtained by TEM (b). Semi-transparent black lines show interfaces to adjacent Si_3N_4 from where the NWell thickness was determined.

the data ensemble required for statistical post-processing. Further information and data on measurement parameters, measurement geometry, and statistical data post-processing can be found in Ref. [20].

Synchrotron UPS measurements were realized at the BaDElPh beamline [21] at the Elettra synchrotron radiation facility in Trieste, Italy, in top-up mode at an electron energy of 2.0 GeV (300 mA electron ring current). Single scans of spectra were recorded over 12 h per NWell sample and subsequently added up for eliminating white noise. Scans for the Si-reference sample were recorded over 2 h and subsequently added up. All NWell samples were excited with photon energies of initially 8.9 eV and of 8.0 eV for subsequent measurements, and a photon flux of ca. $2 \times 10^{12} \text{ s}^{-1}$. The incident angle of the UV beam onto the sample was 50° with respect to the sample surface normal, the excited electrons were collected with an electron analyzer along the normal vector of the sample surface. Energy calibration of the UPS was realized using a tantalum (Ta) stripe in electrical contact to the sample as work function reference. For details on UPS data and measurement, we refer to the supporting information of [1] and the appendix of [2].

The thickness of Si-NWells and its adjacent SiO_2 layers were measured using an ACCURION nanofilm ep4se ellipsometer [22] using a Mueller matrix approach [23–25]. Additional thickness measurements of the Si NWells and top SiO_2 were carried out by Transmission Electron Microscopy (TEM) on selected samples to confirm and/or calibrate ellipsometry measurements, see to representative NWell image in Fig. 1(b). All TEM samples were

capped with a protective 100 nm thick SiO_2 -layer to facilitate the preparation of X-sections by the focused ion beam (FIB) technique using a FEI Strata FIB 205 workstation. Some samples were further thinned by a Fischione NanoMill. TEM analysis of the X-sections was performed at a FEI Tecnai F20 TEM operated at 200 kV at the Central Facility for Electron Microscopy, RWTH Aachen University, and at the spherical aberration corrected FEI Titan 80-300 TEM operated at 300 kV at Ernst Ruska-Centre, Forschungszentrum Jülich [26].

C. Density Functional Theory (DFT) Calculations

Real space calculations were carried out with a molecular orbital basis set (MO-BS) and Hartree-Fock (HF)/DFT methods, employing the GAUSSIAN09 program package [27] with the GaussView program [28] for visualization. Initially, the MO-BS wavefunction ensemble was tested and optimized for describing the energy minimum of the system (variational principle; stable = opt) with the HF method [29–31]. Exact exchange interaction inherent to HF is crucial in obtaining accurate bond geometries, see supporting information of [1]. As MO-BS, we used the Gaussian type 3-21G MO-BS [32]. This HF/3-21G route was used for the structural optimization of approximants to obtain their most stable configuration (maximum integral over all bond energies); root mean square (RMS) and peak force convergence limits were $15.3 \text{ meV } \text{Å}^{-1}$ and $23.1 \text{ meV } \text{Å}^{-1}$, (300 and $450 \mu\text{Ha}/a_{\text{B},0}$), respectively. Optimized geometries were used to calculate their electronic structure by testing and optimizing the MO-BS wavefunction ensemble with the non-local hybrid DF B3LYP [33–35], its modified form featuring the Coulomb Attenuation Method (CAM-B3LYP) for more accurate asymptotic non-local exchange interactions [36], and the HSE06 hybrid DF with its parameters from 2006 [37]. As MO-BS, we used the Gaussian type 6-31G(d) MO-BS which contains d-polarization functions (B3LYP/6-31G(d)) [38] for all chemical elements. For all calculations, tight convergence criteria were set to the self-consistent field routine and no symmetry constraints to MOs were applied. Ultrafine integration grids were used throughout. The supporting information of [1, 39] contain detailed accuracy assessments.

III. RESULTS

A. Qualitative Explanation of the NESSIAS Effect

When a common boundary between two different solids with a bandgap is formed, an interface charge transfer (ICT) occurs [40], generating an interface dipole which may shift the electron work function of both materials with respect to the intrinsic solid-vacuum interface [40, 41]. The solid which accumulates extrinsic electrons

experiences an electronic structure shift to lower binding energies E_{bind} , hence to E_{vac} , the other solid which provides the electronic charge experiences an electronic structure shift in the opposite direction. When LNS i-Si is coated with 1 ML SiO_2 or Si_3N_4 , the ICT provides about the same amount of electrons to O and N as main interface anions in OH and NH_2 groups [2], see to top section in Table I. We would thus expect a nearly iden-

TABLE I. Electronic structure data of Si_x NCs terminated with OH or NH_2 (\equiv 1 ML SiO_2 , Si_3N_4) or 1.5 ML SiO_2 or Si_3N_4 , see [2] for details, showing the NC size d_{NC} , cumulative charge transferred from the Si NC into the dielectric $\sum q_{\text{ICT}}$, and HOMO and LUMO energies E_{HOMO} , E_{LUMO} .

approximant	d_{NC} [nm]	$\sum q_{\text{ICT}}$ [e]	E_{HOMO} [eV]	E_{LUMO} [eV]
$\text{Si}_{10}(\text{NH}_2)_{16}$	0.72	-4.20	-4.02	-0.50
$\text{Si}_{10}(\text{OH})_{16}$		-4.51	-5.31	-2.08
$\text{Si}_{35}(\text{NH}_2)_{36}$	1.10	-10.10	-3.85	-0.66
$\text{Si}_{35}(\text{OH})_{36}$		-10.35	-5.26	-2.46
$\text{Si}_{84}(\text{NH}_2)_{64}$	1.48	-18.51	-3.64	-0.69
$\text{Si}_{84}(\text{OH})_{64}$		-18.52	-5.03	-2.43
$\text{Si}_{165}(\text{NH}_2)_{100}$	1.85	-29.36	-3.62	-0.69
$\text{Si}_{165}(\text{OH})_{100}$		-29.17	-5.10	-2.63
$\text{Si}_{286}(\text{NH}_2)_{144}$	2.22	-42.41	-3.66	-0.82
$\text{Si}_{286}(\text{OH})_{144}$		-43.06	-4.77	-2.72
$\text{Si}_{455}(\text{NH}_2)_{196}$	2.59	-58.12	-3.58	-0.90
$\text{Si}_{455}(\text{OH})_{196}$		-58.84	-4.67	-2.59
Si_{10} in 1.5 ML Si_3N_4	0.72	-4.27	-4.02	-0.21
Si_{10} in 1.5 ML SiO_2		-5.22	-5.67	-2.26
Si_{35} in 1.5 ML Si_3N_4	1.10	-9.23	-3.72	-0.73
Si_{35} in 1.5 ML SiO_2		-10.86	-5.42	-2.76
Si_{84} in 1.5 ML Si_3N_4	1.48	-16.60	-3.54	-0.93
Si_{84} in 1.5 ML SiO_2		-19.30	-5.32	-2.89
Si_{165} in 1.5 ML Si_3N_4	1.85	-25.91	-3.54	-0.75
Si_{165} in 1.5 ML SiO_2		-30.17	-5.19	-2.63
Si_{286} in 1.5 ML Si_3N_4	2.22	-37.24	-3.23	-1.02
Si_{286} in 1.5 ML SiO_2		-43.89	-5.19	-2.74

tical shift of the LNS i-Si electronic structure in accord with interface dipole theory.

However, measurements of Si NCs [39] and nanowells (NWells) [1–3], and DFT calculations of Si NCs [2, 42, 43] and nanowires (NWires) [1] show a very different behavior. Energies of the lowest unoccupied MO (LUMO) E_{LUMO} , and E_{HOMO} listed in Table I show that Si NCs coated with SiO_2 experience a shift to higher E_{bind} , and Si NCs coated in Si_3N_4 experience a shift to lower E_{bind} . This contradiction to interface dipole theory can be resolved when looking at the quantum chemical properties of the chemical elements involved. Such elements are LNS i-Si as the cation providing electrons, and in particular N or O as the anion receiving such electrons. Relevant properties of the anions are the electronegativity (EN) and resulting ionicity of bond (IOB) to Si, the ionization energy E_{ion} , the electron affinity for the neutral anion X^0 , and the electron affinity of the anion ionized with one electron X^- , see Table II. We focus on N and

O as anions to explain the origin of the NESSIAS effect.

TABLE II. Electronegativity (EN) of the ligand elements, resulting ionicity of bond (IOB) to Si, first ionization energy (E_{ion}), electron affinity in neutral state (X^0) and ionized with one negative charge (X^-). Values are from [44], except X^- .

element	EN*	IOB to Si	E_{ion}	X^0	X^-
		[%]	[eV]	[eV]	[eV]
Si	1.74	0	8.15	-1.38	
B	2.01	2	8.30	-0.28	+5.58 [45] [†]
H	2.20	5	13.60	-0.76	+5.85 [46] [×]
C	2.50	13	11.26	-1.26	+9.03 [46] [×]
N	3.07	36	14.53	+0.07	+8.30 [47] [†]
O	3.50	54	13.36	-1.46	+8.03 [48] [×]
F	4.10	75	17.42	-3.40	+7.69 [46] [×]
S	2.44	12	10.36	-2.08	+6.12 [46] [×]

* Allred & Rochow † measured × calculated

Table II shows that N has a much more positive X^0 and still more positive X^- than O, while its IOB to Si is ca. 2/3 of the value O provides. This lower IOB and thus the charge of the ICT *per bond* q_{ICT} is nearly cancelled out by N in Si_3N_4 having 3/2 interface bonds to Si on average due to its trivalent configuration. Thus, values of the cumulative charge transferred to the main anions $\sum q_{\text{ICT}}$ for NCs of same size embedded into 1 ML SiO_2 -vs. Si_3N_4 are nearly equal. The situation changes when the dielectric embedding increases from 1 to 1.5 ML [2], see bottom section of Table I. For 1.5 ML SiO_2 , $\sum q_{\text{ICT}}$ increases for SiO_2 -embedding, though this increase drops from ca. 16 % for Si_{10} NCs to ca. 2 % for Si_{286} NCs. We also see a slight shift of E_{HOMO} towards E_{vac} at Si_{286} and Si_{455} NCs, and a shift of E_{LUMO} towards E_{vac} for Si_{455} NCs, indicating an ICT saturation for 1 ML SiO_2 , and thereby a saturation of NESSIAS at this NC size and embedding. Such saturation cannot be seen for an embedding in 1.5 ML SiO_2 . Looking at NCs embedded in 1 ML Si_3N_4 , we see that $\sum q_{\text{ICT}}$ has lower values when compared to the same NC in 1 ML SiO_2 , whereby the difference diminishes from ca. -7 % for Si_{10} NCs to ca. -1 % for Si_{455} NCs. There is no additional shift of E_{HOMO} and E_{LUMO} away from E_{vac} , strongly suggesting that the NESSIAS effect is not saturated with 1 ML Si_3N_4 for Si_{455} NCs. For 1.5 ML Si_3N_4 -embedding, $\sum q_{\text{ICT}}$ drops notably from a slight overshoot of ca. 2 % for Si_{10} NCs to -12 % for a Si_{286} NC, dropping accordingly more when compared to Si NCs in 1.5 ML SiO_2 . Although $\sum q_{\text{ICT}}$ is the lowest for 1.5 ML Si_3N_4 -embedding, the values of E_{HOMO} and E_{LUMO} relative to E_{vac} remain virtually unchanged when compared to embedding in 1 ML Si_3N_4 . We found the same result from DFT where two Si NCs ranging from 0.7 to 1.9 nm size (Si_{10} to Si_{165}) were calculated within one approximant, one of which was embedded in SiO_2 , and the other in Si_3N_4 , with 3 ML of dielectric between them [1, 2], see also Ref. [20] for details. We thus can state for SiO_2 -embedding that the NESSIAS effect is rather spatially compact and comes

out of saturation fairly quickly with increasing LNS i-Si system size. For Si_3N_4 -embedding, the NESSIAS effect is spatially distributed and the electronic shift is rather smooth, extending over a wider range of LNS i-Si system size. In order to understand this peculiar electronic structure, we look at a sketch combining spatial atomic orbital (AO) distribution and energy levels, see Fig. 2. Arguably, the delocalizing impact of N *vs.* the localizing

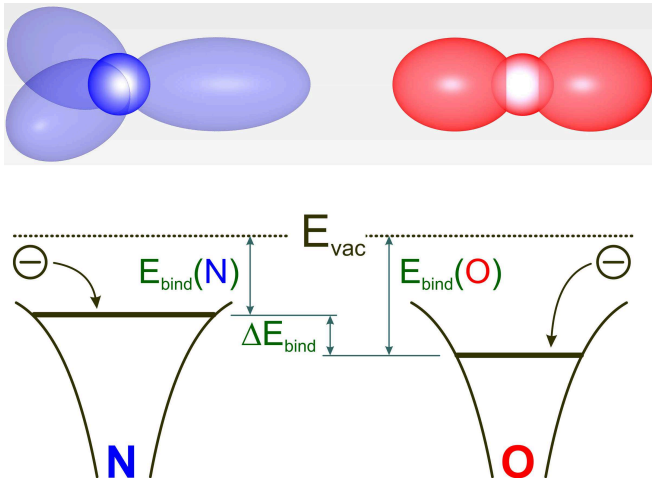


FIG. 2. Relevant quantum chemical properties of N and O shown in spatial space and energy. The top graph shows the spatial extension of frontier occupied AOs. N and in particular O attract electrons from afar due to their high EN. The key difference between N and O is given by the *local* electronic properties: N delocalizes extrinsic electrons due to its positive X^0 and X^- ; O localizes such electrons with its more negative X^0 and X^- . The bottom graph shows the consequence in the energy picture: frontier AOs (and their anti-/non-bonding counterparts) shift to lower E_{bind} for Si_3N_4 -embedding, while frontier AOs for SiO_2 -embedding shift to higher E_{bind} .

impact of O onto their acquired electronic charge is the key to the NESSIAS effect. We can interpret a decreased $\sum q_{\text{ICT}}$ for N as a partial reflection of q_{ICT} back into the LNS i-Si. These observations are supported by a decreasing $\sum q_{\text{ICT}}$ per NC size when going from 1 to 1.5 ML Si_3N_4 -embedding, being confirmed indirectly by experimental results of Si_3N_4 - *vs.* SiO_2 -embedded Si NWells, see Section III D 1 and Fig. 8. The atomistic nature of the NESSIAS implies a short impact length in accord with other near-field effects such as significant electron tunneling [49]. For LNS i-Si, the extension of the NESSIAS is *ca.* 1.3 to 1.8 nm per plane interface [1–3].

B. Analytic Relation of the NESSIAS Effect with the HOMO Energy

We consider interfaces constituted by single bonds, such as between Si/ SiO_2 and Si/ Si_3N_4 . A detailed derivation of the equations below and the use E_{ion} , X^0 and X^- of the interface main anion of the considered ligand group together with the average charge of the main anion $q_{\text{main}}^{\text{avg}}$

as boundary values are given in Appendix Section A. Here, we focus on results to express the binding energy of interface bonds as a function of the parameter $\Lambda_{\text{main}}^{q(\text{main})}$. The average charge of the main anion constituting the ligands to Si NCs $q_{\text{main}}^{\text{avg}}$ is derived from DFT calculations and presents the only non-analytic input to $\Lambda_{\text{main}}^{q(\text{main})}$. We calculate the parameter for a negative charge transfer to the main anion – which is the most likely case –

$$\Lambda_{\text{main}}^{q(\text{main})} = (1 - |q_{\text{main}}^{\text{avg}}|)^{5/2} X_{\text{main}}^0 + \underbrace{|q_{\text{main}}^{\text{avg}}|^{5/2} X_{\text{main}}^-}_{\text{due to negative ionization}} \quad \forall q_{\text{main}}^{\text{avg}} \leq 0 \quad (1)$$

and a positive charge transfer to the main anion of the ligand (or dielectric)

$$\Lambda_{\text{main}}^{q(\text{main})} = (1 - |q_{\text{main}}^{\text{avg}}|)^{5/2} X_{\text{main}}^0 - \underbrace{|q_{\text{main}}^{\text{avg}}|^{5/2} E_{\text{ion, main}}}_{\text{due to positive ionization}} \quad \forall q_{\text{main}}^{\text{avg}} \geq 0. \quad (2)$$

The parameter $\Lambda_{\text{main}}^{q(\text{main})}$ describes the binding energy of the interface bond and is proportional to E_{HOMO} , or the energy of the valence band maximum E_V for sufficiently large LNS i-Si systems like NWells evaluated in Section III D 1. We can thus use $\Lambda_{\text{main}}^{q(\text{main})}$ to predict the NESSIAS as a function of the embedding dielectric, thereby providing optimum combinations of Si and dielectrics per design to meet the desired functionality of VLSI electronic devices as briefly discussed below. Fig. 3 shows the result of

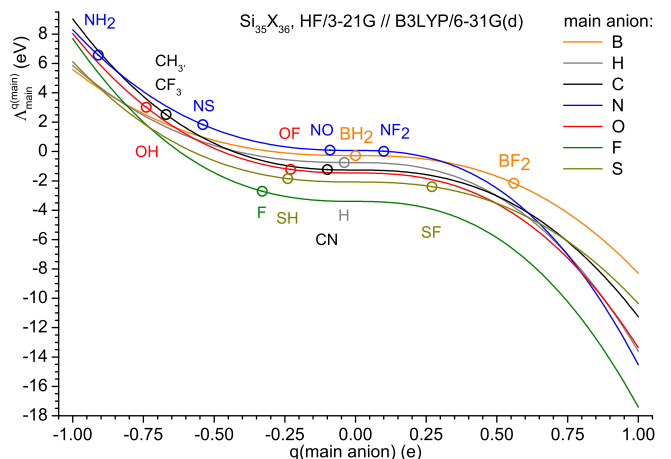


FIG. 3. The parameter $\Lambda_{\text{main}}^{q(\text{main})}$ shown as a function of transferred charge from LNS i-Si to main anion $q(\text{main})$ for all anionic terminations and their possible outer terminations, see Table II. $\Lambda_{\text{main}}^{q(\text{main})}$ for $\text{Si}_{35}\text{X}_{36}$ ($X = \text{ligand}$) is shown per main anion for $q(\text{main}) \in [-1; +1]$, with the respective data point per functional group termination derived from $q_{\text{main}}(\text{DFT})$, see Fig. 5 for corresponding data on electronic structure and $\Lambda_{\text{main}}^{q(\text{main})}$. The difference in $\Lambda_{\text{main}}^{q(\text{main})}$ as per main anion which describes the respective dielectric provides an estimate for the strength of the VB offset ΔE_V between accordingly coated LNS i-Si sections, and can be used for VLSI device design.

Eqs. 1 and 2, together with the data points of all ligands used in DFT calculations of Si_{35} NCs (Section III C). Embedding in SiO_2 *vs.* Si_3N_4 is indeed a good choice for a maximum NESSIAS. Coating LNS i-Si with Fluoride is even more attractive for a maximum electronic structure shift to higher E_{bind} as evident from the bigger difference in $\Lambda_{\text{main}}^{q(\text{main})}$ to Si_3N_4 -embedding. Such differences as per embedding dielectric of LNS i-Si are useful to predict the adequate combination of dielectrics to arrive at type II homojunctions required for VLSI field effect transistors (FETs), *e.g.* using SiO_2 - and Si_3N_4 -embedding, or potentially at band-to-band tunneling (BTBT) FET devices by replacing SiO_2 - with Fluoride-embedding.

Since Si and other semiconductors have a significant inter-atomic charge transfer, the NESSIAS effect will not be limited to a few atomic MLs, providing the basis for its use in VLSI electronics. Within the dielectric, a charge transfer over more than four Si-X (X= O, N) MLs becomes unnotable in particular for SiO_2 embedding [1, 2] because of the strong polar nature of the bonds and immobility of local charges due to charge localization and a rather wide bandgap of SiO_2 and Si_3N_4 .

C. Verification of the Analytic Relation with DFT Simulations

DFT approximants consist of NCs fully terminated with one ligand type. The main anion forms the center of the ligand and the interface bond to the NC. Relevant properties of main anions are listed in Table II. Fig. 4 shows examples of NCs calculated by DFT. The dependence $E_{\text{HOMO}} \propto \Lambda_{\text{main}}^{q(\text{main})}$ can be clearly seen for Si_{35} NCs with a diameter of $d_{\text{NC}} = 1.1$ nm as a function of their surface termination in Fig. 5, where ligands are grouped in accord with their main anion, and specific outer terminations where applicable, arranged for increasing EN from left to right. Recently, H-terminated 1.1 nm size Si NCs were processed by a top-down design [50]. For Si NCs fully terminated with BF_2 , CF_3 , NF_2 , and OF ligands, $\Lambda_{\text{main}}^{q(\text{main})}$ does not appear to follow E_{HOMO} as accurately. This behavior is explained in Ref. [20]. All other terminations are described accurately by $\Lambda_{\text{main}}^{q(\text{main})} \propto E_{\text{HOMO}}$.

We extended calculations of Si_{35} NCs to other hybrid DFs, the Heyd-Scuseria-Ernzerhof DF with its 2006 parametrization (HSE06) [37], and the B3LYP DF complemented with the Coulomb Attenuation Method (CAM-B3LYP) [36]. Detailed results of such calculations are listed in Ref. [20], further corroborating the accuracy of $\Lambda_{\text{main}}^{q(\text{main})}$ in predicting E_{HOMO} .

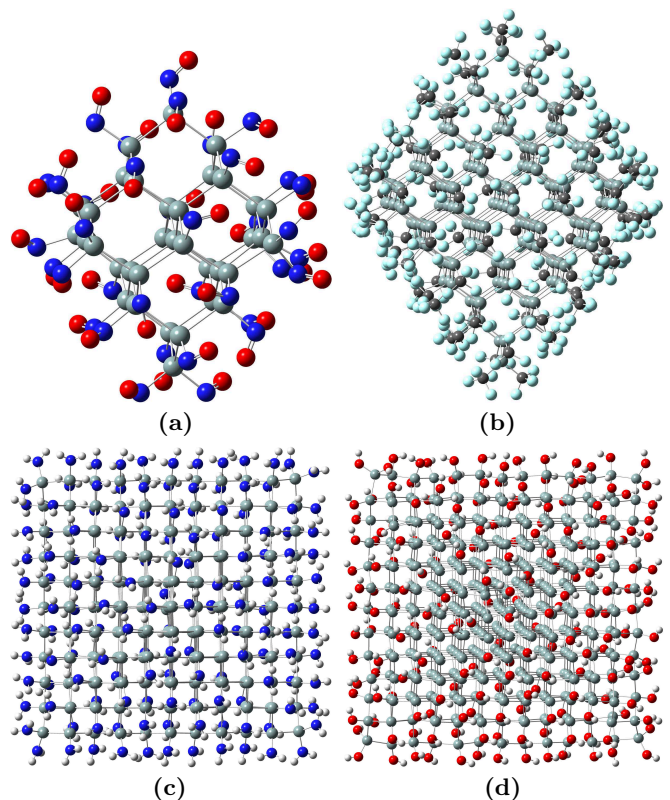


FIG. 4. Examples of structurally optimized approximants of which DFT data are shown in Figs. 3 and 5 and in Ref. [20]: (a) $\text{Si}_{35}(\text{NO})_{36}$, (b) $\text{Si}_{165}(\text{CF}_3)_{100}$, shown along the $\langle 110 \rangle$ vector class, and (c) $\text{Si}_{286}(\text{NH}_2)_{144}$, and (d) $\text{Si}_{455}(\text{OH})_{196}$, shown along the $\langle 001 \rangle$ vector class. Atom colors are white (H), anthracite (C), blue (N), red (O), and gray (Si). Further Data on other DFs and NC sizes can be found in Ref. [20].

D. Details of the NESSIAS Effect in Si NWells from Experiment

1. Calibrating the NESSIAS by Measuring the Intrinsic Valence Band Edge with Synchrotron UPS

First data of SiO_2 - and Si_3N_4 -embedded Si NWells were obtained by measuring the VB maximum (leading edge) of bulk Si and embedded Si NWells using scan ensembles of synchrotron UPS [1–3] with their statistic data, whereby the VB maximum is located at Γ point; $E_{\text{V}} = E_{\text{V}}^{\Gamma}$. We now discuss the fine structure of UPS spectra, revealing a sub-edge which can be assigned to the Van Hove singularity of bulk Si at the L point in the BZ with its energy E_{V}^{L} [51, 52]. For NWells with $d_{\text{Well}} \leq 5$ nm, the VB subband structure becomes increasingly perturbed by QC. An assignment of subband Van Hove singularities near E_{V} becomes a function of d_{Well} and of specific high symmetry points in the electronic DOS along non-orthogonal \mathbf{k} -directions of the NWell plane, in particular X and M, see Ref. [20]. Fig. 6 illustrates the change in VB electronic structure with the shrinking size of LNS i-Si using experimentally derived values. We fo-

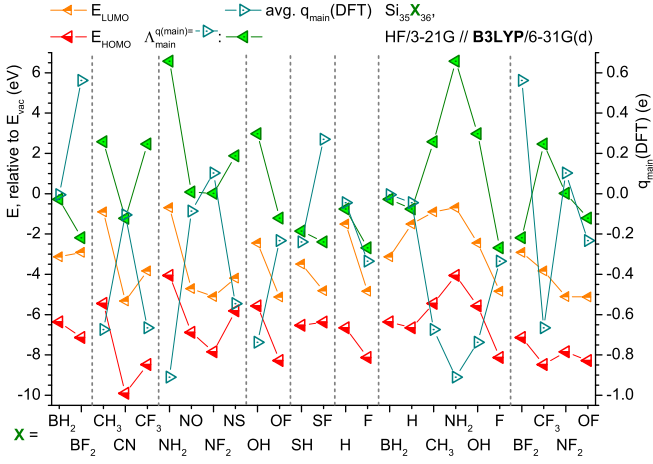


FIG. 5. Energies E_{HOMO} and E_{LUMO} with $\Lambda_{\text{main}}^{q(\text{main})}$ and $q(\text{main})$ (right scale) relative to E_{vac} for Si_{35} NCs (1.1 nm size) as a function of complete surface termination noted at the abscissa. Electronic structure calculations were carried out as indicated in legend, see text for details. More data obtained by the CAM-B3LYP and HSE06 DFs for Si_{35} , and for Si NCs up to 2.6 nm size (Si_{455}) are available in Ref. [20].

cus on the energy offset between Γ and L point for bulk Si, and between Γ and X, M points for thin NWells, generally expressed by the term $\Delta E_{\text{V}}^{\text{VanHove}}$.

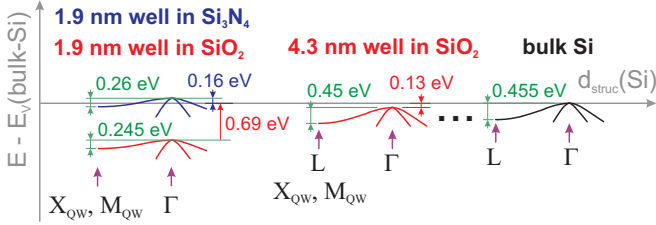


FIG. 6. Sketch of the electronic structure of the VB top with $\Delta E_{\text{V}}^{\text{VanHove}}$, evolving with decreasing d_{Well} . Subbands are shown for bulk Si (black), for NWells in SiO_2 (red), and for NWells in Si_3N_4 (blue). Values of the VB shift relative to the VB edge of bulk Si were taken from the respective least residual fit in Fig. 8. Values of $\Delta E_{\text{V}}^{\text{VanHove}}$ are shown in dark green, see to Fig. 7, and to Ref. [20] for more details.

Fig. 7 shows that $\Delta E_{\text{V}}^{\text{VanHove}}$ does not depend on the embedding dielectric as should be the case for a pure QC phenomenon with sufficiently high potential walls (i.e. band offsets between respective bulk phases) [53], *cf.* Fig. 10(a). When QC sets in with decreasing d_{Well} , the energy offset between VB-DOS extrema at Γ and adjacent Van Hove singularities $\Delta E_{\text{V}}^{\text{VanHove}}$ diminishes as E_{V}^{Γ} is shifted to higher binding energies. Since the adjacent Van Hove singularities already have higher binding energies with respect to the VB maximum, they do not experience a notable energy shift due to QC even for the minimum energetic distance of $\Delta E_{\text{V}}^{\text{VanHove}} \approx 0.2$ eV for NWells with $d_{\text{Well}} = 1.1$ nm, see Fig. 7. We can therefore take $\Delta E_{\text{V}}^{\text{VanHove}}$ as a good estimate for the shift of $E_{\text{V}}^{\Gamma} = E_{\text{V}}$

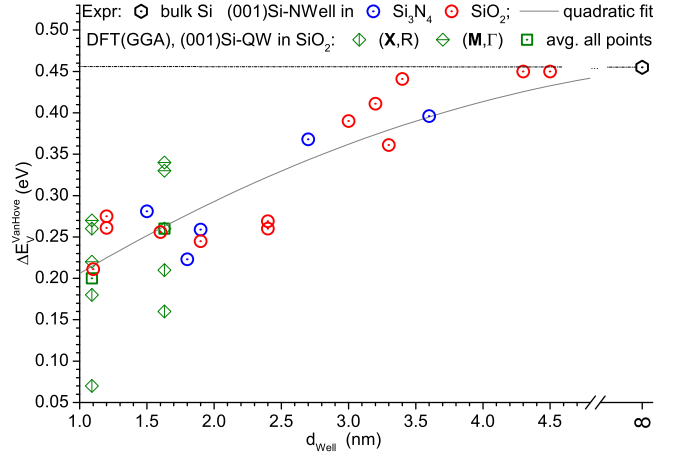


FIG. 7. Energy difference between VB-DOS extrema at Γ point and adjacent Van Hove singularities $\Delta E_{\text{V}}^{\text{VanHove}}$ as function of d_{Well} embedded in SiO_2 (red dots) and in Si_3N_4 (blue dots). The gray line is a quadratic-hyperbolic least residuals fit, the black hexagonal symbol shows the bulk value of $\Delta E_{\text{V}}^{\text{VanHove}}$; please observe abscissa break. Green symbols denote Van Hove singularities for Si NWells in SiO_2 with $d_{\text{Well}} = 1.09$ and 1.63 nm, embedded in 1.92 nm thick SiO_2 barriers as calculated by DFT with periodic boundary conditions [54]. Small rhomboid symbols show local Van Hove singularities per \mathbf{k} -point, the big square symbol per d_{Well} shows their average value. For details on UPS measurement and data retrieval from published DFT calculations, see Ref. [20].

to higher binding energies due to QC only. Interestingly, DFT-GGA calculations of Si NWell superlattices (SLs) with 1.9 nm thick SiO_2 barriers [54] yield very similar values of $\Delta E_{\text{V}}^{\text{VanHove}}(d_{\text{Well}})$, *cf.* Fig. 7 and discussion in Ref. [20]. Yet, the energy offset $\Delta E_{\text{V}}^{\text{VanHove}}$ derived from UPS does not reflect the unperturbed QC case due to its finite energy difference, accounting for some uncertainty of the Van Hove singularity with higher binding energy [53] as the reference level for $\Delta E_{\text{V}}^{\text{VanHove}}$. Still, this deviation on the order of 1 meV is further diminished by the DOS in the Brillouin zone (BZ) at L point in bulk Si being *ca.* five-fold bigger as compared to the DOS at Γ point, see to UPS data for surface-cleaned bulk Si (Fig. S7, Ref. [20]). Local deviations due to stress/strain and the deviation of d_{Well} of *ca.* ± 0.2 nm around its nominal value have a more significant impact on $\Delta E_{\text{V}}^{\text{VanHove}}$, see Fig. 7. Hence, $\Delta E_{\text{V}}^{\text{VanHove}}$ as measured by UPS is an accurate estimate of VB QC. We introduce a VB maximum as a function of NWell thickness,

$$E_{\text{V}}^{\text{QC}}(d_{\text{Well}}) = E_{\text{V}}(\text{bulk Si}) + \left[E_{\text{V}}^{\Gamma}(\text{bulk Si}) - E_{\text{V}}^{\text{L}}(\text{bulk Si}) \right] - \Delta E_{\text{V}}^{\text{VanHove}} \quad (3)$$

$$= 5.17 \text{ eV} + 0.455 \text{ eV} - \Delta E_{\text{V}}^{\text{VanHove}}.$$

In Fig. 7, a quadratic-hyperbolic least residuals fit was used in accord with QC theory [53] to estimate the shift of E_{V} as a function of d_{Well} .

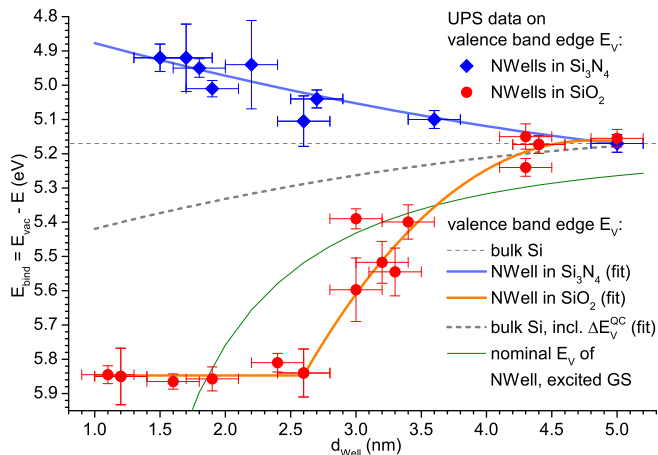


FIG. 8. Synchrotron UPS data of the VB maxima of Si NWells embedded in SiO_2 (red symbols) and Si_3N_4 (blue symbols). Error bars show standard deviations in thickness and energy. Orange and light blue lines provide a least square residual fit to $E_V(d_{\text{Well}})$ for SiO_2 - and Si_3N_4 -embedding, respectively. The thin dashed gray line shows E_V of bulk Si, the thick dashed gray line shows E_V with intrinsic QC $E_V^{\text{QC}}(d_{\text{Well}})$, see text for details. The green line shows E_V of the nanowell for photon absorption (including exciton binding energy, excluding lattice relaxation) as per existing theory.

We present all UPS data together with $E_V^{\text{QC}}(d_{\text{Well}})$ in Fig. 8. The energy offset due to the NESSIAS as per embedding dielectric is clearly visible, saturating for SiO_2 -embedding for $d_{\text{Well}} \leq 2.6$ nm, while steadily growing with decreasing d_{Well} for Si_3N_4 -embedding. The VB offset between 1.6 nm thick Si NWells coated with Si_3N_4 *vs.* SiO_2 is $\Delta E_V \approx 0.95$ eV, facilitating charge carrier separation on a massive scale in analogy to a steep p/n junction induced by impurity doping. Before discussing the full electronic structure of embedded Si NWells with experimental data, we revisit the discussion of the quantitative NESSIAS impact due to Si_3N_4 *vs.* SiO_2 .

With $E_V^{\text{QC}}(d_{\text{Well}})$, we have a true reference level to investigate on a quantitative base how the NESSIAS affects Si NWells per embedding dielectric. To that effect, we calculate the absolute value of the difference between $E_V^{\text{QC}}(d_{\text{Well}})$ and the VB maximum $E_V(d_{\text{Well}})$ per embedding dielectric, *viz.* $|\Delta E_V^{\text{NESSIAS}}| = |E_V^{\text{QC}}(d_{\text{Well}}) - E_V(d_{\text{Well}})|$ *cf.* Fig. 9. As already emerging from Fig. 8, $|\Delta E_V^{\text{NESSIAS}}|$ becomes saturated for $d_{\text{Well}} \leq 2.6$ nm for NWells in SiO_2 . The strong localization of extrinsic electrons from the NWell at the O atoms in SiO_2 has two effects. Due to the small localization volume which is limited to the immediate proximity of O atoms, see Section III A, these atoms undergo electrostatic screening. Thereby, the ICT from the NWell to SiO_2 is self-limiting. The NWell undergoes a rather strong positive ionization, increasing the attractive Coulomb force which works against the ICT. Together with the screened O atoms, the cumulative ICT charge $\sum q_{\text{ICT}}$ thus *decreases* for $d_{\text{Well}} < 2.6$ nm, whereby its partition per Si NWell atom

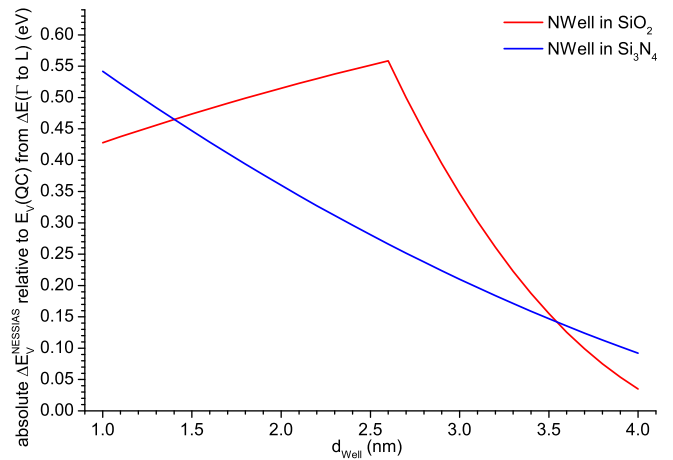


FIG. 9. Absolute values of $\Delta E_V^{\text{NESSIAS}}$ as a function of d_{Well} relative to $E_V^{\text{QC}}(d_{\text{Well}})$, using the least square residual fits of VB edges of Fig. 8. The NESSIAS becomes saturated for NWells in SiO_2 around $d_{\text{Well}} = 2.6$ nm, but not for $d_{\text{Well}} \geq 1.0$ nm for NWells in Si_3N_4 , see text for further discussion.

still increases. The latter statement is straightforward to see when comparing $|\Delta E_V^{\text{NESSIAS}}|$ of $d_{\text{Well}} = 2.6$ nm with its value at half the NWell thickness. There, $|\Delta E_V^{\text{NESSIAS}}|$ decreased from its maximum of 0.56 eV at $d_{\text{Well}} = 2.6$ nm not by about 0.28 eV as would be the case for a constant NWell ionization, but by a mere 0.10 eV, accounting for a further increase of the positive ionization per Si NWell atom. We note, though, that the electronic DOS of the VB over energy is not constant. Further decrease in $|\Delta E_V^{\text{NESSIAS}}|$ may occur due to an increased DOS at the energy where $E_V^{\text{QC}}(d_{\text{Well}})$ resides. The situation is very different for Si_3N_4 -embedding, where $|\Delta E_V^{\text{NESSIAS}}|$ is constantly increasing for a decreasing d_{Well} , getting close to the saturation limit of SiO_2 -embedding. This behavior is in accord with the quantum-chemical properties of N, see Section III A. It is uncertain whether we can proceed to Si_3N_4 -embedded NWells with $d_{\text{Well}} < 1.1$ nm to find a saturation limit in experiment should it exist. What we do know from experiment is that the constant increase of $|\Delta E_V^{\text{NESSIAS}}|$ with decreasing d_{Well} results from the electron-attractive, yet delocalizing nature of N which does not suffer from a saturation due to a much bigger volume which can be utilized by N to accommodate extrinsic electrons. As discussed in Section III A, this peculiar behavior also results in a part of the ICT to be reflected back into the NWell as a consequence of the decreased binding energy of extrinsic electrons at N atoms, thereby shifting the electronic structure of the NWell and LNS i-Si in general towards E_{vac} .

We have stated in Section III A that 1 ML SiO_2 can keep the NESSIAS saturated for a ratio of LNS i-Si atoms per interface bond of $N_{\text{IF}}/N_{\text{Si}} = 196/455 \approx 0.43$ for Si NCs. Fig. 8 shows that this saturation is left around $d_{\text{Well}} = 2.6$ nm which corresponds to ca. 19 atomic ML of (001)Si or 38 Si atoms and eight interface bonds per unit cell area, resulting in $N_{\text{IF}}/N_{\text{Si}} = 8/38 \approx 0.21$. As-

suming an exponential decay in charge transfer through SiO_2 when moving away from the interface, we arrive at the estimate of ca. 3 ML or 0.9 nm SiO_2 [1, 39] after which the NESSIAS does not increase significantly anymore by increasing the thickness of SiO_2 . While this is good news for the VLSI technology where ultrathin SiO_2 layers are required to chemically passivate LNS i-Si and to establish the primary layer of gate dielectrics, there is little chance to extend a saturated NESSIAS in Si beyond $d_{\text{Well}} = 2.6$ nm. For Si_3N_4 -embedding, the delocalizing impact of N yields to a NESSIAS smeared out over d_{Well} , with no saturation present for $d_{\text{Well}} \geq 1.5$ nm.

2. A First Glimpse on the Full NESSIAS Picture

We recently started to measure the energy of the conduction band edge E_C of Si NWells embedded in SiO_2 by means of X-ray Absorption Spectroscopy in Total Fluorescence Yield mode (XAS-TFY) [3]. An initial sample of a Si_3N_4 -coated NWell gave us a very first glimpse on the electronic structure of Si NWells of comparable thickness as a function of their embedding. We thus focus here on two NWell samples with $d_{\text{Well}} = 1.9 \pm 0.2$ nm and the respective embedding. Details of other SiO_2 -coated NWells can be found in [3] and its supporting information, representative scans and statistical data of both samples used here can be found in Ref. [20]. The obtained experimental data for E_V and E_C are shown together with the bulk phases of Si, SiO_2 , and Si_3N_4 in Fig. 10(a). Fig. 10(b) shows a combination of both NWell samples, with the resulting band diagram as per experimental data from Fig. 10(a). Obviously, we can induce a strong type II homo-junction [60] in LNS i-Si merely by coating with SiO_2 *vs.* Si_3N_4 .

The band structures of bulk solids shown in Fig. 10(a) yield to further insights into the NESSIAS effect. The band offsets between the bulk phases of Si and SiO_2 as well as Si and Si_3N_4 are somewhat asymmetric. A strong shift of E_C , E_V to higher binding energies occurs for SiO_2 . For Si_3N_4 , we see a smaller shift to lower binding energies. Both observations are in accord with our discussion of O and N *vs.* Si in Section III A. We thus can track the NESSIAS effect all the way to the bulk phase of the respective dielectric. As a consequence, the entire electronic structure of LNS i-Si such as a sufficiently thin NWell moves towards a more symmetric band offset with the respective dielectric when the NESSIAS effect becomes significant.

From above discussion, the question of a LNS i-Si size limit arises below which it starts to behave like the embedding dielectric to a degree where they depart from the properties of semiconducting Si. Further research efforts will be required to provide a thickness estimate around which the NESSIAS effect can be put to best use for technological applications from the viewpoint of LNS i-Si system size. Moreover, recent DFT calculations [3] showed that other group IV semiconductors such as C and Ge –

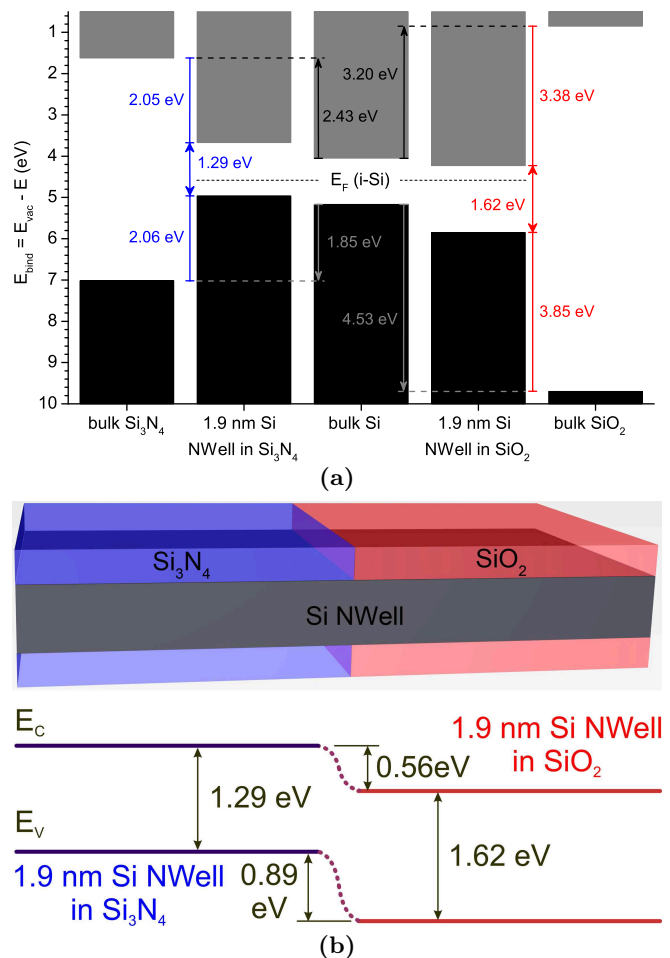


FIG. 10. (a) Regions of fundamental band gaps for – left to right – bulk Si_3N_4 [1, 55–57], a 1.9 nm Si-NWell in Si_3N_4 , intrinsic bulk Si [1, 58], a 1.9 nm Si-NWell in SiO_2 , and bulk SiO_2 [1, 57–59]. Band offsets to dielectrics are shown by labelled red (blue) lines for NWells in SiO_2 (Si_3N_4), and in gray/black for bulk Si. Band edges given contain values of bulk solids from experiment, data for NWells were obtained by UPS and XAS-TFY, see to text, Ref. [20] and to [1–3] with respective supplements. (b) Layer system comprising a 1.9 nm thick Si NWell coated with 1.0 nm Si_3N_4 and SiO_2 (top), and its band diagram with energies in units of eV (bottom), derived from experimental data in graph (a).

and presumably their alloys SiC and SiGe – strongly respond to the NESSIAS, offering a much broader impact on VLSI device design beyond LNS Si.

IV. CONCLUSIONS

We quantitatively demonstrated that an energy shift of electronic states defining the CB and VB edge of low nanoscale intrinsic Si (LNS i-Si) exists, being considerably different from commonly assumed energy positions. The underlying Nanoscale Electronic Structure Shift Induced by Anions at Surfaces (NESSIAS) is brought about

by the embedding dielectric, whereby N in the form of Si_3N_4 and O in the form of SiO_2 are of particular scientific and technological interest. We explained the underlying quantum chemical processes of the NESSIAS which mainly reside with the anion of the dielectric, namely its ability to attract extrinsic electrons such as from LNS i-Si from afar (electronegativity EN defining the ionicity of bond to Si), and its ability to localize extrinsic electrons in its immediate vicinity (electron affinity X). Both, O and N attract extrinsic electrons from i-Si via an interface charge transfer. While such electrons get strongly localized at O with its highly negative X^0 , they get delocalized around N due to its X^0 being positive. Therefore, electronic states experience a shift to higher binding energies with O as an interface anion, while the delocalization of extrinsic electrons in the immediate vicinity of N reflects such states partly back to the LNS i-Si, lowering their binding energy. Due to these quantum chemical properties, the NESSIAS saturates rather quickly as a function of SiO_2 thickness, while still increasing for Si_3N_4 -coatings beyond three atomic MLs. The NESSIAS thus results in an electronic structure shift towards (away from) E_{vac} for Si_3N_4 - (SiO_2 -) embedding. Hence, LNS i-Si systems like NWires [3] or NWells can be flooded by holes (Si_3N_4 -coated) or electrons (SiO_2 -coated), a property which readily offers the formation of a type II (p/n) homojunction in LNS i-Si.

We introduced an analytic parameter as a function of the ionization of the main interface anion $\Lambda_{\text{main}}^{q(\text{main})}$ which correctly predicts the HOMO energy E_{HOMO} of the LNS i-Si system as a function of the main interface anion, and verified its accuracy with three different hybrid DFs. As main anions to Si, we evaluated the entire 1st period of the periodic table and S, with all of these main anions terminated by all possible outer atoms to form ligands. Using $\Lambda_{\text{main}}^{q(\text{main})}$ to predict the NESSIAS as a function of the dielectric coating, we obtain optimum combinations of Si and dielectrics per design to meet the desired functionality of VLSI electronic devices. Such predictions are useful in particular for ultra-low power VLSI devices and ultimate cryogenic electronics as with NESSIAS, no dopants are required for a p/n junction to exist.

Band edges of 1.9 nm thick Si NWells measured by UPS and XAS-TFY revealed band offsets due to Si_3N_4 -vs. SiO_2 -coating of $\Delta E_C = 0.56$ eV and $\Delta E_V = 0.89$ eV. The band gap energies were $E_{\text{gap}} = 1.29$ eV for Si_3N_4 - and $E_{\text{gap}} = 1.62$ eV for SiO_2 -embedding, respectively. Looking at the evolution of experimental E_C and E_V values with decreasing d_{Well} , we showed that the band offsets of the NWells to the respective dielectric get more symmetric. It emerged that the absolute position of E_C and E_V residing with the respective dielectric is also a function of the quantum chemical properties at the origin of the NESSIAS. Detecting the NESSIAS in DFT calculations and in experiment requires the evaluation of E_C and E_V on an *absolute* energy scale. *e.g.* their position to E_{vac} . The impact length for a saturation of the NESSIAS is ca. 1.5 ± 0.2 nm per plane interface, result-

ing in $\leq 3.0 \pm 0.4$ nm thick Si NWells and $\leq 5.5 \pm 0.8$ nm thick Si NWires [3]. This short impact length and the lack of published DFT calculations and measurements with an *absolute* energy calibration are the likely reasons why the NESSIAS has not been detected until recently [1, 39, 42]. With VLSI approaching ultrathin fins and NWires, device dimensions are currently advancing into the thickness ranges mentioned above. It should therefore be of high interest to the VLSI research community to carry out device-related research, in particular in the light of the prospective ultra-low power demand and low temperature functionality given by the NESSIAS effect.

ACKNOWLEDGMENTS

D. K. acknowledges the 2018 Theodore-von-Kàrmàn Fellowship of RWTH Aachen University, Germany. M. F., N. W. and J. K. acknowledge support by the Impulse and Networking Fund of the Helmholtz Association. D.H. acknowledges funding via a Heisenberg grant by the Deutsche Forschungsgemeinschaft (DFG, German Research Foundation), project #434030435. I.P., F.B., and E.M. acknowledge funding from EUROFEL project (RoadMap Esfri) and thank Federico Salvador (IOM-CNR) for technical support. The authors acknowledge Elettra Sincrotrone Trieste for providing access to its synchrotron radiation facilities (through proposals #20165089, #20180054, #20190057, #20200079, #20205084, #20215072, and #20215081), and thank L. Sancin for technical support at Elettra, and Simone Dal Zilio for advise and use of the Micro and Nano fabrication facility FNF at IOM-CNR. D. K. and S. C. S. acknowledge the National Computational Infrastructure (NCI) for the generous computing resources allocated on the Gadi supercomputer, Australian National University, Canberra, Australia.

Appendix A: Derivation of the quantum Chemical Parameter Λ to describe E_{HOMO} for Various Interface Ligands/Dielectrics

We set out by relating E_{ion} , X^0 and X^- of the interface main anion of the ligand group to the average charge transferred from the LNS Si to the main anion $q_{\text{main}}^{\text{avg}}$:

$$\Lambda_{\text{main}}^{q(\text{main})} = (1 - |q_{\text{main}}^{\text{avg}}|)X_{\text{main}}^0 + \underbrace{|q_{\text{main}}^{\text{avg}}|X_{\text{main}}^-}_{\text{due to negative ionization}} \quad \forall q_{\text{main}}^{\text{avg}} \leq 0 \quad (\text{A1})$$

$$\Lambda_{\text{main}}^{q(\text{main})} = (1 - |q_{\text{main}}^{\text{avg}}|)X_{\text{main}}^0 - \underbrace{|q_{\text{main}}^{\text{avg}}|E_{\text{ion, main}}}_{\text{due to positive ionization}} \quad \forall q_{\text{main}}^{\text{avg}} \geq 0 \quad (\text{A2})$$

For $q_{\text{main}}^{\text{avg}} = 0$, we arrive at the trivial result that the regular electron affinity X^0 applies. The term $E_{\text{ion, main}}$

stands for the ionization energy of the main anion which is counted positive towards E_{vac} ; X^0 and X^- are counted negative (positive) when going below (above) E_{vac} . For avoiding confusion with the signs of $q_{\text{main}}^{\text{avg}}$, we use its absolute value. For $q_{\text{main}}^{\text{avg}} \geq 0$, we include $E_{\text{ion, main}}$ due to X_{main}^0 being increasingly substituted by $E_{\text{ion, main}}$, since a localized electron would have to fill up the vacant valency before it starts to present a real negative charge in the sense of an electron affinity. The influence of the cation is implicitly included in above equations via $q_{\text{main}}^{\text{avg}}$ which depends on E_{ion} of the nominal cation (semiconductor structure), and in a few cases from its electron affinities X^0 , X^- when charge is transferred from the embedding material to the LNS semiconductor system, as is the case for SF_2 or BF_2 ligands in Fig. 5. This atypical behavior is due to the peculiar quantum chemical nature of F in ligands, see Ref. [20] for further discussion.

Equations A1 and A2 establish the principal relation to describe the NESSIAS effect. We now work out the dependence of $\Lambda_{\text{main}}^{q(\text{main})}$ on $q_{\text{main}}^{\text{avg}}$. To this end, we need a Coulomb term which is a function of $q_{\text{main}}^{\text{avg}}$ localized at the main anion, leading to a Coulomb functional (Coulomb field) of a quasi-point charge distributed in a local atomic potential of the main anion, *viz.* $\mathbf{F}_{\text{Coul}}(q_{\text{main}}^{\text{avg}}[\mathbf{r}])$. This approach requires a local potential to accommodate $q_{\text{main}}^{\text{avg}}$ which is given by the Lennard-Jones potential [61]

$$V_{\text{LJ}}(\mathbf{r}) = 4\epsilon \left[\left(\frac{\sigma}{\mathbf{r}} \right)^{12} - \left(\frac{\sigma}{\mathbf{r}} \right)^6 \right], \quad (\text{A3})$$

with ϵ being the minimum energy of the potential well, and σ being the inter-particle distance which refers to the inter-electron distance of the electron pair forming the single bond per main anion to the Si NC, see Fig. 11. The potential minimum $V_{\text{LJ}}/\epsilon = -1$ occurs at $\mathbf{r}_m = 2^{1/6}\sigma$, with σ set to 0.05 nm as an example. In our investigation of the anion impact, we will focus on the *attractive* part of $V_{\text{LJ}}^{\text{attr}}$, namely $V_{\text{LJ}}^{\text{attr}} = -(\sigma/\mathbf{r})^6$ which can enable or prevent the localization of an external electron, depending on the charge state and outer termination of the main anion. Since we do not have the exact inter-particle distance of the two electrons forming the Si-anion bond (nor does this make much sense from a quantum mechanical viewpoint), and ϵ varies as per anion type and its charge state, we work with proportionalities in analogy to solving a partial fraction decomposition by comparison of coefficients [62]. The scaling of such proportionality relations are given by E_{ion} , X^0 , and X^- at $q_{\text{main}}^{\text{avg}} = +1$, 0, and -1 , respectively. We approximate $V_{\text{LJ}}^{\text{attr}}(\mathbf{r})$ by a hard-sphere potential of $V \rightarrow \infty$ at $\mathbf{r} = \mathbf{r}_m = 2^{1/6}\sigma$, and $V(\mathbf{r}) = V_{\text{LJ}}^{\text{attr}}(\mathbf{r})$ for $\mathbf{r} \geq 2^{1/6}\sigma$. The exact and the approximated well potentials integrated over their outward spatial extension \mathbf{r} should be possibly identical to ensure an adequate description of charge localization. As shown in Appendix Section A1, the spatial extension of the well of the approximated $V_{\text{LJ}}^{\text{attr}}$ deviates from V_{LJ} by a mere 2.9%. No boundary conditions are needed as integration limits since we scale the proportionality relations with quantum chemical properties as per above,

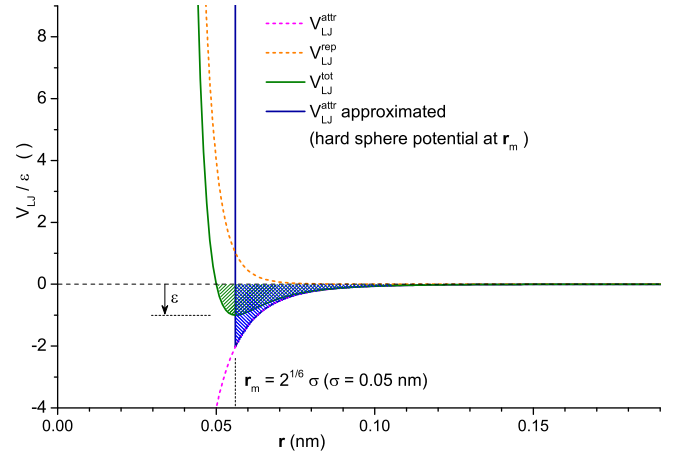


FIG. 11. Lennard-Jones potential V_{LJ} and hard-sphere potential to approximate the attractive part $V_{\text{LJ}}^{\text{attr}}$ used for deriving $\Lambda_{\text{main}}^{q(\text{main})}$. The normalized V_{LJ}/ϵ (dark green line) consists of a repulsive nuclear term $V_{\text{LJ}}^{\text{rep}}$ (orange dashed line) and an attractive Coulomb term $V_{\text{LJ}}^{\text{attr}}$ (magenta dashed line). The hard-sphere potential has $V \rightarrow \infty$ for $\mathbf{r} \leq \mathbf{r}_m$, and $V_{\text{LJ}}^{\text{attr}}$ for $\mathbf{r} \geq \mathbf{r}_m$ (blue line). The green hatched area marks the potential well of V_{LJ} , the blue hatched area marks the well area of the approximated $V_{\text{LJ}}^{\text{attr}}$ used in integration of $q_{\text{main}}^{\text{avg}}$ over \mathbf{r} .

merely requiring the correct description of all variables in powers of \mathbf{r} . For the accumulated (or depleted) charge $q_{\text{main}}^{\text{avg}}[\mathbf{r}]$, we integrate over its location, *viz.*

$$q_{\text{main}}^{\text{avg}}[\mathbf{r}] = q_{\text{main}}^{\text{avg}} \int V_{\text{LJ}}^{\text{attr}} d\mathbf{r} \quad (\text{A4})$$

$$\propto \frac{q_{\text{main}}^{\text{avg}}}{\mathbf{r}^5}$$

Due to their comparatively big distance as compared to the localized anionic charge, we can approximate the Coulomb field of the main anion onto NC atoms as a point charge, yielding

$$\mathbf{F}_{\text{Coul}}(q_{\text{main}}^{\text{avg}}[\mathbf{r}]) = e \frac{q_{\text{main}}^{\text{avg}}}{4\pi\epsilon_0 \mathbf{r}^2} \propto \frac{q_{\text{main}}^{\text{avg}}}{\mathbf{r}^2}, \quad (\text{A5})$$

where e is the elementary charge presenting the probe charge into which the Coulomb field exerts its impact, and ϵ_0 is the permittivity constant of vacuum. We thus get $\mathbf{F}_{\text{Coul}}(q_{\text{main}}^{\text{avg}}[\mathbf{r}])$ describing an *energy* gradient which will become more apparent below.

Next, we provide a gauge for the interface impact on an atomic scale, *i.e.* an area density of potential energy due to charge accumulation/depletion at the main anion which influences the electronic structure of the NC atoms. Such density is given by the quotient of the Coulomb impact onto the NC and the charge localization at the main anion:

$$\frac{\text{field due to } q_{\text{main}}^{\text{avg}} \text{ at NC}}{\text{location of } q_{\text{main}}^{\text{avg}} \text{ at anion}} = \frac{\mathbf{F}_{\text{Coul}}(q_{\text{main}}^{\text{avg}})|_{\text{NC}}}{q_{\text{main}}^{\text{avg}}[\mathbf{r}]|_{\text{anion}}}$$

$$\propto \frac{1/\mathbf{r}^2}{1/\mathbf{r}^5} = \mathbf{r}^{5/2} \quad (\text{A6})$$

Equation A6 presents a Coulomb pressure onto the NC in analogy to a force constant conveying the exertion of force onto a mechanical system: An increased $q_{\text{main}}^{\text{avg}}$ results in an increased $\mathbf{F}_{\text{Coul}}(q_{\text{main}}^{\text{avg}})$ which will impact upon the probe charge e , whereby the location of $q_{\text{main}}^{\text{avg}}$ resides with $V_{\text{LJ}}^{\text{attr}}$, thereby scaling the impact of the quantum chemical properties of the main anion, *viz.* X_{main}^0 , X_{main}^- , and E_{ion} . With relation A6 describing an area density of Coulomb energy, we substitute $q_{\text{main}}^{\text{avg}}$ in Eqs. A1 and A2 with $(q_{\text{main}}^{\text{avg}})^{5/2}$, ending up with

$$\Lambda_{\text{main}}^{q(\text{main})} = (1 - |q_{\text{main}}^{\text{avg}}|)^{5/2} X_{\text{main}}^0 + \underbrace{|q_{\text{main}}^{\text{avg}}|^{5/2} X_{\text{main}}^-}_{\text{due to negative ionization}} \quad \forall q_{\text{main}}^{\text{avg}} \leq 0 \quad (\text{A7})$$

$$\Lambda_{\text{main}}^{q(\text{main})} = (1 - |q_{\text{main}}^{\text{avg}}|)^{5/2} X_{\text{main}}^0 - \underbrace{|q_{\text{main}}^{\text{avg}}|^{5/2} E_{\text{ion, main}}}_{\text{due to positive ionization}} \quad \forall q_{\text{main}}^{\text{avg}} \geq 0, \quad (\text{A8})$$

which are equivalent to Eqs. 1 and 2 in the main article.

1. Comparison of Well Potentials – V_{LJ} vs. Approximated $V_{\text{LJ}}^{\text{attr}}$

For comparing both well areas, we integrate the respective potential over \mathbf{r} with its integration limits, yielding

$$\begin{aligned} A_{\text{Well}}(V_{\text{LJ}}) &= \int_{\sigma}^{\infty} \left(\frac{\sigma}{\mathbf{r}} \right)^{12} - \left(\frac{\sigma}{\mathbf{r}} \right)^6 d\mathbf{r} \quad (\text{A9}) \\ &= \left[-\frac{\sigma^{12}}{11 \cdot \mathbf{r}^{11}} + \frac{\sigma^6}{5 \cdot \mathbf{r}^5} \right]_{\sigma}^{\infty} \\ &= -\frac{6}{55} \sigma \end{aligned}$$

for the well formed by the Lennard-Jones potential, and

$$\begin{aligned} A_{\text{Well}}(V_{\text{LJ}}^{\text{attr}} \text{ approx.}) &= \int_{2^{1/6}\sigma}^{\infty} - \left(\frac{\sigma}{\mathbf{r}} \right)^6 d\mathbf{r} \quad (\text{A10}) \\ &= \left[\frac{\sigma^6}{5\mathbf{r}^5} \right]_{2^{1/6}\sigma}^{\infty} \\ &= -\frac{1}{5 \cdot 2^{5/6}} \sigma \end{aligned}$$

for the well described by the hard sphere potential approximating $V_{\text{LJ}}^{\text{attr}}$. With $A_{\text{Well}}(V_{\text{LJ}})$ being the exact potential, we arrive at

$$\frac{A_{\text{Well}}(V_{\text{LJ}}^{\text{attr}} \text{ approx.})}{A_{\text{Well}}(V_{\text{LJ}})} = \frac{-55\sigma}{-6 \cdot 5 \cdot \sigma \cdot 2^{5/6}}, \quad (\text{A11})$$

yielding 1.0289, *i.e.* a deviation of the approximated well area from the exact Lennard-Jones well of ca. 2.9 %.

-
- [1] D. König, D. Hiller, N. Wilck, B. Berghoff, M. Müller, S. Thakur, G. D. Santo, L. Petaccia, J. Mayer, S. Smith, and J. Knoch, *Beilstein J. Nanotech.* **9**, 2255 (2018).
- [2] D. König, N. Wilck, D. Hiller, B. Berghoff, A. Meledin, G. D. Santo, L. Petaccia, J. Mayer, S. Smith, and J. Knoch, *Phys. Rev. Appl.* **12**, 045050 (2019).
- [3] D. König, M. Frentzen, N. Wilck, B. Berghoff, I. Piš, S. Nappini, F. Bondino, M. Müller, S. Gonzalez, G. D. Santo, L. Petaccia, J. Mayer, S. Smith, and J. Knoch, *ACS Appl. Mater. Interfaces* **13**, 20479 (2021).
- [4] It is interesting to note in this context that the VLSI technology nodes do not reflect the physical gate length. We have a planar MOSFET *model* shrunken to a size where it *would perform* as the fin-FET of the respective technology node [63].
- [5] T. D. Ladd, F. Jelezko, R. Laflamme, Y. Nakamura, C. Monroe, and J. L. O'Brien, *Nature* **464**, 45 (2010).
- [6] N. Garcia-Castello, S. Illera, J. D. Prades, S. Ossicini, A. Cirera, and R. Guerra, *Nanoscale* **7**, 12564 (2015).
- [7] K. Jarolimek, E. Hazrati, R. A. de Groot, and G. A. de Wijs, *Phys. Rev. Appl.* **8**, 014026 (2017).
- [8] S. Ossicini, I. Marri, M. Amato, M. Palumbo, E. Canadell, and R. Rurali, *Faraday Discuss.* **222**, 217 (2020).
- [9] S. Halilov, M. L. Belayneh, M. A. Hossain, A. A. Abdallah, B. Hoex, and S. N. Rashkeev, *RSC Adv.* **10**, 22377 (2020).
- [10] D. König, D. Hiller, and S. Smith, *Phys. Stat. Sol. B* **259**, 2100549 (2022).
- [11] B. G. Lee, D. Hiller, J.-W. Luo, O. E. Semonin, M. C. Beard, M. Zacharias, and P. Stradins, *Adv. Funct. Mater.* **22**, 3223 (2012).
- [12] N. H. Thoan, K. Keunen, V. V. Afanas'ev, and A. Stesmans, *J. Appl. Phys.* **109**, 013710 (2011).
- [13] D. K. Basaa, M. Bose, and D. N. Bose, *J. Appl. Phys.* **87**, 4324 (2000).

- [14] S. Jung, D. Gong, and J. Yi, *SOLMAT* **95**, 546 (2011).
- [15] B. E. Deal and A. S. Grove, *J. Appl. Phys.* **36**, 3770 (1965).
- [16] F. W. Kern and C. A. Deckert, in *Thin film processes*, edited by V. L. Vossen and W. Kern (Academic Press, New York, 1978) Chap. 5, pp. 411–413.
- [17] G. Kräuter, A. Schumacher, and U. Gösele, *Sensors and Actuators A* **70**, 271 (1998).
- [18] M. Zangrando, M. Zacchigna, M. Finazzi, D. Cocco, R. Rochow, and F. Parmigiani, *Rev. Sci. Instr.* **75**, 31 (2004).
- [19] L. Stebel, M. Malvestuto, V. Capogrosso, P. Sigalotti, B. Ressel, F. Bondino, E. Magnano, G. Cautero, and F. Parmigiani, *Rev. Sci. Instr.* **82**, 123109 (2011).
- [20] See Supplemental Material for additional data on DFT calculations for Si NCs of various sizes and surface terminations using different DFs, details on UPS measurements including DFT data supporting $\Delta E_V^{\text{VanHove}}$, details on XAS-TFY measurements.
- [21] L. Petaccia, P. Vilmercati, S. Goronikov, M. Barnaba, A. Bianco, D. Cocco, C. Masciovecchio, and A. Goldoni, *Nucl. Instr. Meth. in Phys. Res. A* **606**, 780 (2009).
- [22] “Nanofilm_ep4, MICROSCOPIC THIN FILM METROLOGY AND VISUALIZATION,” (2020), https://www.accurion.com/accurion_broschuere_EP4_201906.pdf, accessed August 24, 2022, see page 6 ‘self-assembled monolayers’.
- [23] H. Mueller, *J. Opt. Soc. Am.* **38**, 661 (1948).
- [24] R. M. A. Azzam, *J. Opt. Soc. Am.* **68**, 1756 (1978).
- [25] S. N. Savenkov, in *Light Scattering Reviews*, Vol. 4, edited by A. A. Kokhanovsky (Springer, Berlin, 2009) Chap. 3, pp. 71–119.
- [26] A. Thust, J. Barthel, and K. Tillmann, *Journal of large-scale research facilities JLSRF* **2**, A41 (2016), DOI: 10.17815/jlsrf-2-66.
- [27] GAUSSIAN09, *Revision D.01*, M. J. Frisch, et. al., Gaussian, Inc., Wallingford, CT (2012).
- [28] R. Dennington, T. Keith, and J. Millam, “GaussView 5.0.8,” (2009).
- [29] D. R. Hartree, *Proc. Cambr. Phil. Soc.* **24**, 89 (1928).
- [30] D. R. Hartree, *Proc. Cambr. Phil. Soc.* **24**, 111 (1928).
- [31] V. Fock, *Zeitschr. Phys.* **61**, 126 (1930), in German.
- [32] M. S. Gordon, J. S. Binkley, J. A. Pople, W. J. Pietro, and W. J. Hehre, *J. Am. Chem. Soc.* **104**, 2797 (1982).
- [33] A. D. Becke, *Phys. Rev. A* **38**, 3098 (1988).
- [34] C. Lee, W. Yang, and R. G. Parr, *Phys. Rev. B* **37**, 785 (1988).
- [35] A. D. Becke, *J. Chem. Phys.* **98**, 5648 (1993).
- [36] T. Yanai, D. P. Tew, and N. C. Handy, *Chem. Phys. Lett.* **393**, 51 (2004).
- [37] A. V. Krukau, O. A. Vydrov, A. F. Izmaylov, and G. E. Scuseria, *J. Chem. Phys.* **125**, 224106 (2006).
- [38] M. M. Francl, W. J. Pietro, W. J. Hehre, J. S. Binkley, D. J. DeFrees, J. A. Pople, and M. S. Gordon, *J. Chem. Phys.* **77**, 3654 (1982).
- [39] D. König, D. Hiller, S. Gutsch, and M. Zacharias, *Adv. Mater. Interfaces* **1**, 1400359 (2014).
- [40] W. Mönch, *Semiconductor Surfaces and Interfaces*, 3rd ed. (Springer, Berlin, 2001).
- [41] I. H. Campbell, S. Rubin, T. A. Zawodzinski, J. D. Kress, R. L. Martin, D. L. Smith, N. N. Barashkov, and J. P. Ferraris, *Phys. Rev. B.* **54**, R14321 (1996).
- [42] D. König, J. Rudd, M. A. Green, and G. Conibeer, *Phys. Rev. B* **78**, 035339 (2008).
- [43] D. König, J. Rudd, M. A. Green, and G. Conibeer, *Solar Energy Mater. & Solar Cells* **93**, 753 (2009).
- [44] A. F. Holleman, E. Wiberg, and N. Wiberg, *Lehrbuch der Anorganischen Chemie*, 101st ed. (Walter deGruyter, Berlin, 1995) in German.
- [45] M. Scheer, R. C. Bilodea, and H. K. Haugen, *Phys. Rev. Lett.* **80**, 2562 (1998).
- [46] Y. Guo and M. A. Whitehead, *Can. J. Chem.* **68**, 1585 (1990).
- [47] J. E. Huheey, ed., *Inorganic Chemistry*, 3rd ed. (Harper & Row, New York, 1983) appendix 5.
- [48] A. P. Ginsberg and J. M. Miller, *J. Inorg. Nucl. Chem.* **7**, 351 (1958).
- [49] B. Brar, G. D. Wilk, and A. C. Seabaugh, *Appl. Phys. Lett.* **69**, 2728 (1996).
- [50] P. P. Shirahata, J. Nakamura, J. i. Inoue, B. Ghosh, K. Nemoto, Y. Nemoto, M. Takeguchi, Y. Masuda, M. Tanaka, and G. A. Ozin, *Nano Lett.* **20**, 1491 (2020).
- [51] J. R. Chelikowsky, T. J. Wagener, J. H. Weaver, and A. Jin, *Phys. Rev. B* **40**, 9644 (1989).
- [52] L. Ley, S. Kowalczyk, R. Pollack, and D. A. Shirley, *Phys. Rev. Lett.* **29**, 1088 (1972).
- [53] L. I. Schiff, *Quantum Mechanics*, 3rd ed. (McGraw-Hill, Singapore, 1968) pp. 39.
- [54] P. Carrier, L. J. Lewis, and M. W. C. Dharma-wardana, *Phys. Rev. B* **65**, 165339 (2002).
- [55] H. Kurata, H. Masataka, and Y. Osaka, *Jap. J. Appl. Phys.* **20**, L811 (1981).
- [56] A. Iqbal, W. B. Kackson, C. C. Tsai, J. W. Allen, and C. W. B. Jr., *J. Appl. Phys.* **61**, 2947 (1987).
- [57] J. W. Keister, J. E. Rowe, J. J. Kolodziej, H. Niimi, T. E. Madey, and G. Lucovsky, *J. Vac. Sci. Tech. B* **17**, 1831 (1999).
- [58] E. H. Nicollian and J. R. Brews, *MOS (Metal Oxide Semiconductor) Physics and Technology* (Wiley, New York, 1982).
- [59] H. Ibach and J. E. Rowe, *Phys. Rev. B* **10**, 710 (1974).
- [60] P. Harrison, *Quantum Wells, Wires and Dots*, 2nd ed. (Wiley, Chichester, 2009) pp. 11.
- [61] S. Elliott, *The Physics and Chemistry of Solids* (Wiley & Sons, Chichester, 1998).
- [62] E. Zeidler, W. Hackbusch, and H. R. Schwarz, *Oxford User’s Guide to Mathematics* (Oxford University Press Inc., New York, 2004) translated from German by Bruce Hunt.
- [63] (2016), J.-P. Collinge, Tyndall National Institute, Cork, Ireland; private communication.